A NUMERICAL CALCULATION OF STORM TIDES INDUCED BY A TROPICAL STORM IMPINGING ON A CONTINENTAL SHELF

CHESTER P. JELESNIANSKI

U.S. Weather Bureau, Washington, D.C.

ABSTRACT

The transient phase of a storm surge generated by an idealized tropical storm in a coastal area is investigated by numerical means. Linearized forms of the storm surge equations of motion are used without bottom friction. Open water boundaries are considered in a basin with varying depth. The basin is separated into regions of differing grid sizes that give a greater density of points in shallow water.

It is found that inflow of wind across the isobars is significant in storm surge generation, whereas the motion of the storm plays a smaller role. The pressure gradient gives only static heights in deep water with three times the static height at the coast on passage of a moderately moving storm.

1. INTRODUCTION

The interplay of atmospheric forces and boundary effects that govern the variation of sea level at a coastal strip in an ocean basin are too complex to permit an analytic solution in any but the simplest of real problems. Many decades will have elapsed before sufficient empirical data are collected to permit the development of satisfactory forecasting techniques based on purely statistical considerations. Consequently it is natural that a numerical approach to the hurricane storm surge prediction problem should be employed. Several studies of this type, see for example Hansen [2], Platzman [7], Miyazaki et al. [4] and Miyazaki [5], have been carried out. Although the design of numerical schemes requires meticulous care, the results for the special problems considered encourage a continuing study toward the desirable end of developing methods that can be used in routine forecasts and other applications.

The numerical approach presents several serious problems such as a proper specification of the wind and pressure fields sufficiently far in advance of the storm's approach, and a proper specification of the depth field and coastal boundaries (these frequently change during the course of the storm as a result of erosion processes and flooding). In addition some rather difficult computational problems are involved. This paper considers a few of these computational problems and demonstrates that, in spite of the

severe difficulties, results of general usefulness appear to be possible.

The two most severe computational difficulties result from the small horizontal scale of the phenomena being considered relative to the oceans in which they occur, and the great variability in ocean depths. The mesh length used in numerical calculation must be small enough to permit a description of both the storm and the water level disturbances which form in response to the storm. The available theories determining stability and convergence of numerical solutions require that Δt, the time increment, be less than some constant multiplied by $\Delta s/c$, where Δs is the mesh length, and c is the greatest phase speed of any wave in the system. In the storm surge problem, $c = (gD_m)^{1/2}$, where g is the acceleration of gravity and D_m is the maximum depth in any space interval. Thus in deep water, prohibitively small time increments may be necessary for the small mesh lengths required.

In this study efforts were made to obviate the above difficulties by formulating open boundary conditions and by developing a system whereby a basin is broken into sub-regions. The mesh length of the sub-region containing the shore-line boundary is much shorter than those in deep water, while the largest time increment applicable equally to all the sub-regions is used. Since the natural boundaries of the ocean may extend thousands of miles from the coastal area of interest, it appears that calcula-

tions will be practical only if they can be limited to a region comprising only a small fraction of the entire ocean.

In order to learn more about this system a small, highly idealized storm crossing the coast at normal incidence and moderate speed was developed in analytical form. The storm was positioned in a closed basin for which boundary conditions are known exactly, and then on a small sub-basin of the closed basin for which experimental boundary conditions were specified. The closed basin was not an entire ocean but a much smaller idealized basin. The acceptability of the experimental boundary statements was judged on the basis of similarity of results for the experimental open water boundary sub-basin compared to the larger closed basin. The effects of wind and pressure from the storm acting on the basins are shown separately and together. Several numerical expressions had to be investigated before a satisfactory system was derived. Since the available stability theorems could not be applied rigorously, an energy budget was maintained as a check on computational stability.

The tests described indicate that at the coast of an open water boundary basin, the storm surges are in general proportional to those computed for the closed basin. Even if the two sets of calculations had agreed in detail, one should not expect the calculations to be more than approximately proportional to observations since secondary effects such as surface waves cannot be considered explicitly in this model, and the wind and pressure fields as well as the relation of wind speed to wind stress acting on the sea's surface are not known exactly.

Since empirical data on severe storm surges do not exist in abundance, storm surge calculations which are approximately proportional to actual events can be very useful. Such calculations may permit one to determine the segments of greatest and least activity along a coast, as well as the relative activity associated with storms of different sizes approaching the coast with various speeds from different directions. The results would be of immediate qualitative value to the hurricane warning service, and would provide insight on the relative importance of various mechanisms involved in storm surge generation.

With these goals in mind it is appropriate to limit initial considerations to the linearized form of the momentum equations, to use an idealized, but variable, hurricane model, and to omit consideration of bottom friction. This last omission is particularly important at present, since appropriate expressions for the bottom friction force are unknown. One can only hope that the omission does not lead to significant errors during the important generating stage of the storm surge controlled by the force functions.

2. STORM SURGE EQUATIONS AND THEIR NUMERICAL FORM

In a previous report, Harris and Jelesnianski [3] gave the storm surge equations in linear form without bottom

friction as,

$$\frac{\partial U}{\partial t} = -gD(x, y)\frac{\partial h}{\partial x} + fV + {}^{(x)}\tau(x, y, t) \qquad (1)$$

$$\frac{\partial V}{\partial t} = -gD(x, y)\frac{\partial h}{\partial y} - fU + {}^{(y)}\tau(x, y, t) \qquad (2)$$

$$\frac{\partial h}{\partial t} = -\frac{\partial U}{\partial x} - \frac{\partial V}{\partial y} \qquad (3)$$

where

$D =$ depth of basin from the equilibrium surface

$f =$ Coriolis parameter

${}^{(x)}\tau$ ${}^{(y)}\tau =$ force components per unit mass

$h =$ height of undisturbed surface fluid from the undisturbed free surface

$U =$ transport in the x-direction

$V =$ transport in the y-direction

$g =$ gravity acceleration

For all computations in this paper constant values were assigned to the Coriolis parameter and gravity acceleration: $f = 10^{-4}$ sec.$^{-1}$; $g = 32$ ft. sec.$^{-2}$. In this report and in [3], only rectangular basins are considered. At closed boundaries, or vertical walls, only free slip boundary conditions are applied. The corner points between two vertical walls have zero transport. Open boundary conditions are discussed in a later section.

The numerical scheme for the above equations at *interior* points was given as,

$$U_{i,j}^{m+1} = U_{i,j}^{m-1} - gD_{i,j}\frac{\Delta t}{4\Delta s}\begin{vmatrix} -1 & 0 & 1 \\ -2 & 0 & 2 \\ -1 & 0 & 1 \end{vmatrix}h_{i,j}^{m}$$

$$+ \frac{f\Delta t}{8}\begin{vmatrix} 1 & 2 & 1 \\ 2 & 4 & 2 \\ 1 & 2 & 1 \end{vmatrix}V_{i,j}^{m} + 2\Delta t \,{}^{(x)}\tau_{i,j}^{m} \quad (4)$$

$$V_{i,j}^{m+1} = V_{i,j}^{m-1} - gD_{i,j}\frac{\Delta t}{4\Delta s}\begin{vmatrix} 1 & 2 & 1 \\ 0 & 0 & 0 \\ -1 & -2 & -1 \end{vmatrix}h_{i,j}^{m}$$

$$- \frac{f\Delta t}{8}\begin{vmatrix} 1 & 2 & 1 \\ 2 & 4 & 2 \\ 1 & 2 & 1 \end{vmatrix}U_{i,j}^{m} + 2\Delta t \,{}^{(y)}\tau_{i,j}^{m} \quad (5)$$

$$h_{i,j}^{m+1} = h_{i,j}^{m-1} - \frac{\Delta t}{4\Delta s}\left\{\begin{vmatrix} -1 & 0 & 1 \\ -2 & 0 & 2 \\ -1 & 0 & 1 \end{vmatrix}U_{i,j}^{m} + \begin{vmatrix} 1 & 2 & 1 \\ 0 & 0 & 0 \\ -1 & -2 & -1 \end{vmatrix}V_{i,j}^{m}\right\}$$

$$(6)$$

where $U_{i,j}^{m+1} = U(i\Delta s, j\Delta s, m\Delta t)$, etc. The field value, immediately to the right of an array in vertical brackets, represents the middle point of the nine-point grid array. The numbers in the array represent weights attached to the field values at adjacent points. This is a convenient

geometrical shorthand notation for the finite difference operators used in this study. The parallel transport at a closed boundary is determined by operating with an ordinary central difference form on (1)–(2); note that on a closed boundary the Coriolis cross term vanishes. Height values on the boundary points, excluding the corner points, for a variable depth basin were given as,

$$h_{0,j}^m = \frac{4h_{1,j}^m D_{1,j} - h_{2,j}^m D_{2,j} - \dfrac{2\Delta s}{g}[fV_{0,j}^m + {}^{(x)}\tau_{0,j}^m]}{4D_{1,j} - D_{2,j}} \qquad (7)$$

The above is for the left boundary. Similar forms apply for the other walls. Although the above form permits zero depths on the boundaries, this case is not considered because nonlinear terms would then become dominant. Heights on the corner points between two vertical walls were treated as follows,

$$h_{0,0}^m = \frac{\begin{vmatrix} -1 & 0 & -1 \\ 4 & 4 & 0 \\ 0 & 4 & -1 \end{vmatrix}(Dh)_{1,1}^m - \dfrac{4\Delta s}{g}[{}^{(x)}\tau_{0,0}^m + {}^{(y)}\tau_{0,0}^m]}{\begin{vmatrix} -1 & 0 & -1 \\ 4 & 4 & 0 \\ 0 & 4 & -1 \end{vmatrix}D_{1,1}} \qquad (8)$$

The above is for the lower left corner and similar forms apply for the other corners.

A starting procedure for these equations was given in [3]. In this report and in [3], field values are calculated at each grid point for each time interval.

3. GEOMETRY OF A PATCHED GRID SYSTEM

The time interval Δt prescribed by the usual stability criteria of the hyperbolic or wave equation, may be unreasonably small in deep water for small grid spacings. One is thus led to consider the possibility of enlarging the spacing in deep water without altering the spacing in shallow water so that the resulting Δt common to both regions has an operationally reasonable value. Such a system would be advantageous in decreasing the points on the revised grid, would allow a savings in computation time for the larger Δt, and would have a density of points in shallow water where the contour fields are assumed more complex than in deep water.

Two equally wide rectangular grids of different mesh lengths are patched or joined together at a line called a partition line. Figure 1 illustrates a partition line for two grids along the vertical line P. Hereafter it will be assumed that the grid spacing of an adjacent region is twice or one-half that of the first region. The partition line has an odd number of points.

It is readily seen that the numerical scheme defined thus far can be applied to all points of the two grids except the interior points of the partition line. A study of figure 1 shows that for the points encircled, $\odot$, an ordinary central difference form can be used. To determine field
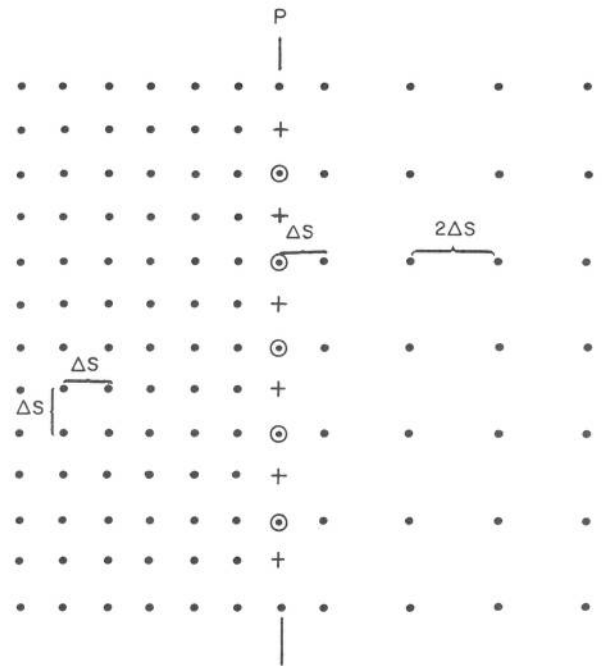

FIGURE 1.—Two rectangular grids joined at a partition line P. The points $\odot$ and $+$ require different finite difference forms in numerical calculations.

values at points marked $+$, a variation of the central difference form was used as follows,

$$\left.\begin{aligned} U_{i,j}^{m+1} &= U_{i,j}^{m-1} - gD_{i,j}\frac{\Delta t}{2\Delta s}\begin{vmatrix} -1 & 0 & 1 \\ 0 & 0 & * \\ -1 & 0 & 1 \end{vmatrix} h_{i,j}^m \\ &\qquad\qquad\qquad + 2\Delta t[fV_{i,j}^m + {}^{(x)}\tau_{i,j}^m] \\[6pt] V_{i,j}^{m+1} &= V_{i,j}^{m-1} - gD_{i,j}\frac{\Delta t}{2\Delta s}\begin{vmatrix} 1 & 0 & 1 \\ 0 & 0 & * \\ -1 & 0 & -1 \end{vmatrix} h_{i,j}^m \\ &\qquad\qquad\qquad - 2\Delta t[fU_{i,j}^m - {}^{(y)}\tau_{i,j}^m] \\[6pt] h_{i,j}^{m+1} &= h_{i,j}^{m-1} - \frac{\Delta t}{2\Delta s}\left\{\begin{vmatrix} -1 & 0 & 1 \\ 0 & 0 & * \\ -1 & 0 & 1 \end{vmatrix}U_{i,j}^m + \begin{vmatrix} 1 & 0 & 1 \\ 0 & 0 & * \\ -1 & 0 & -1 \end{vmatrix}V_{i,j}^m\right\} \end{aligned}\right\} \qquad (9)$$

The symbol $*$ refers to nonexistent points.

Tests made on a partitioned basin with this system of numerical forms proved at first to be inadequate after a few time intervals had elapsed. Because the numerical forms (4)–(6) remove wavelengths of $2\Delta s$ (the smallest recognized by the grid), whereas the forms applied to the points $\odot$ and $+$ have no built-in smoothing device to remove these corrupting waves, it was decided to *replace* the numerically computed field values at the points $\odot$ and $+$ by a separate smoothing procedure to take place *after* completion of the numerical calculations at each time step.

The nature of the partition points does not permit a

nine-point symmetric smoothing routine, but does permit a five-point smoothing routine that at least partially eliminates wavelengths of two grid spacings (Shuman [10]). Smoothing of the field values on the partition line at the end of each time-step calculation was done as follows; for the points $\odot$,

$$\tilde{U}^m_{i,j}, \tilde{V}^m_{i,j}, \tilde{h}^m_{i,j} = \frac{1}{8} \begin{vmatrix} 0 & 1 & * \\ 1 & 4 & 1 \\ 0 & 1 & * \end{vmatrix} U^m_{i,j}, V^m_{i,j}, h^m_{i,j} \qquad (10)$$

for the $+$ points,

$$\tilde{U}^m_{i,j}, \tilde{V}^m_{i,j}, \tilde{h}^m_{i,j} = \frac{1}{8} \begin{vmatrix} 1 & 0 & 1 \\ 0 & 4 & * \\ 1 & 0 & 1 \end{vmatrix} U^m_{i,j}, V^m_{i,j}, h^m_{i,j} \qquad (11)$$

where U, V, h are computed by the appropriate difference forms for points in the bracketed array, and $\tilde{U}, \tilde{V}, \tilde{h}$ replace the numerically calculated field values of the interior partition points before the next time step is begun.

4. A CALCULATION WITH THE PATCHED GRID SYSTEM

Consider the basin of figure 2. The depth is given by,

$$D(x) = -\frac{4b}{L^2} x^2 + \frac{4b}{L} x + c \qquad (12)$$

A preliminary run was performed on a rectangular one-region basin of type shown in figure 2 for the following constants: $c = 15$ ft., $b = 200$ ft., $L = 470$ mi., $\Delta s = 5$ mi., $\Delta t = 200$ sec. The grid was composed of 48×17 points. The fluid in the basin was excited by a simplified forcing function, which was not a function of depth. The forcing function died out after 72 time intervals and the basin was then under free oscillation. The Coriolis term was retained. The energy of the basin, solid line of figure 3a, was computed after each time interval by the method described in [3]; it varied so little under free oscillation that it was not deemed necessary to take this run beyond a total of 100 time intervals.

For a comparison of the above master run with a patched grid system, a partition line was placed at the depth of 104 ft. The grid points then totaled 333 points against 816 in the master run. The time increment used for this patched grid was 320 sec. Figure 3a gives a comparison of the energy for this run (broken line) with the master run (solid line). The energy curve shows very little variation during free oscillation and agrees very well with the energy value of the master run. The broken-dotted curve results from a third run for a one-region basin with all constants the same as the master run except that Δs and Δt were increased to 10 mi. and 320 sec. respectively.

Figure 3b gives energy curves of a smaller basin for runs similar to those that produced figure 3a. L was changed to 430 mi. and Δs, Δt for the master run were 7.5 mi. and 200 sec. respectively; Δt for the patched grid was taken as 400 sec. Details for these runs are not given and
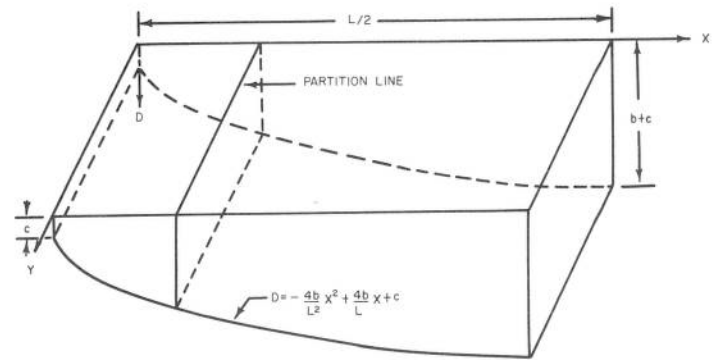

FIGURE 2.—A one-dimensional parabolic depth basin. If two regions of differing grid sizes are used, the partition line patches the regions together.
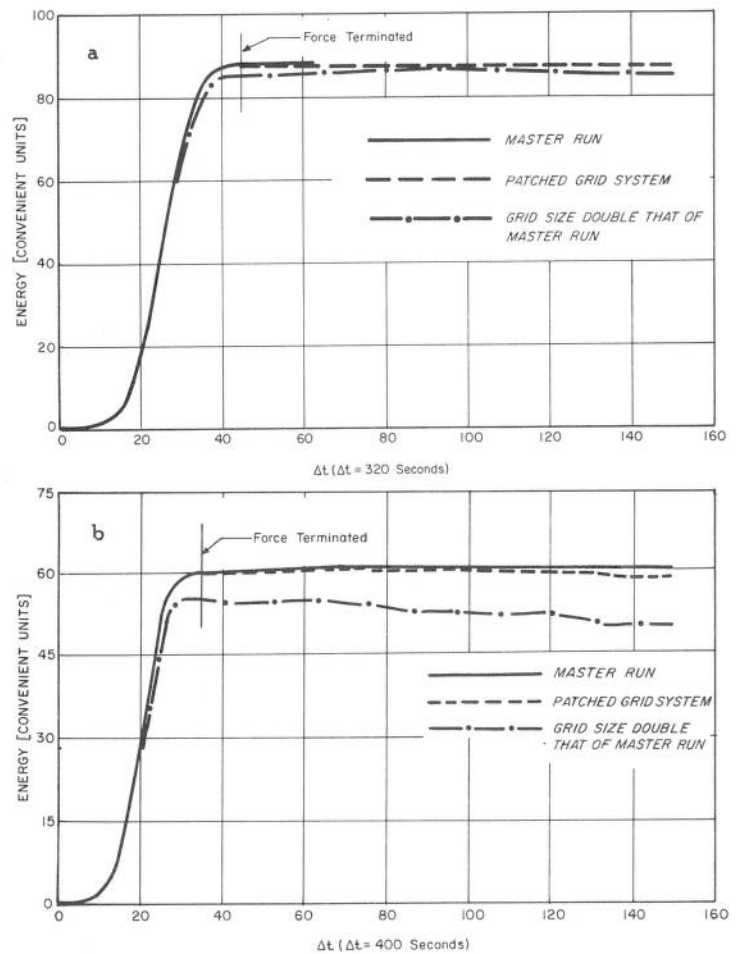

FIGURE 3.—Energy, in convenient units, with time for basins of figure 2 during and after application of a forcing function. (a) Curves for larger basin ($L = 470$ mi.), (b) Curves for smaller basin ($L = 430$ mi.).

figure 3b is inserted only to demonstrate that the patched grid system can serve intermediately between two grid sizes while retaining the best features of both. The energy decrease under free oscillation for the double grid size suggests instability from too large a grid spacing.
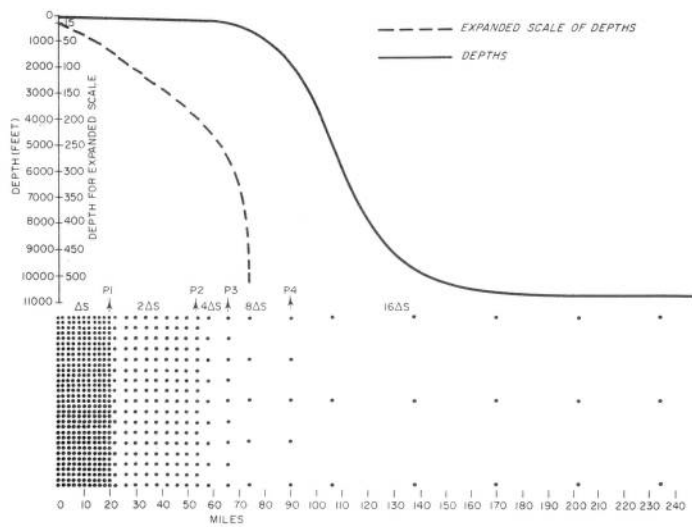
FIGURE 4.—Idealized one-dimensional depths of the ocean basin with distance from the shore. An attendant patched grid system of points for five regions is displayed. This grid system was used in the wind stress calculations.
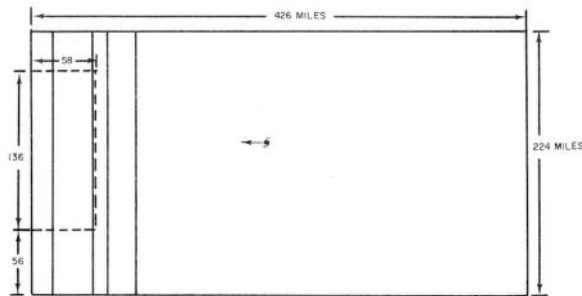

FIGURE 5.—Top view of a closed basin broken into five regions. The broken outline is a two-region sub-basin with three open boundaries. The initial position of a storm is marked by a hurricane symbol. The units are statute miles.

In both basins, the contours of field values for the patched grid runs were continuous without fragmentation. The field values agreed almost identically with those produced by the master runs.

5. A GRID SYSTEM FOR A SECTION OF THE OCEAN BASIN

Figure 4 is a one-dimensional depth profile of a basin composed of a gently sloping continental shelf bounded by a steeply inclined continental slope which in turn is joined to an abyssal plain. This is an idealization of the depth profile off the mid-Atlantic coast of the United States.

A representative sample of patched grid points is displayed in figure 4 for the one-dimensional depth profile broken into five regions. The distance between points in the first region is 2 mi. ($\Delta s = 2$ mi.). The partition lines are numbered P1 to P4. Note that regions 1, 2, and
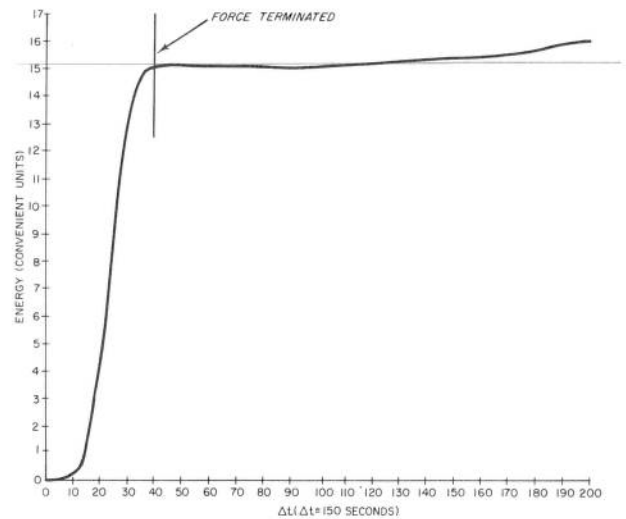

FIGURE 6.—Energy curve, in convenient units, with time for the closed five-region basin of figure 5 during and after application of a wind stress function.

5 have several grid spacings, whereas regions 3 and 4 have only one grid spacing. For the depths assigned to these various regions, a time step of 150 sec. is applicable.

Figure 5 is a top view of an idealized closed basin used in this study. This is only a section of the entire ocean basin. The entire ocean basin is not considered because of program limitations. The depths are those of figure 4 with extreme depths at the right closed boundary. The basin is divided into five regions as illustrated by the solid vertical lines. The dotted outline represents a smaller sub-basin with three open boundaries which was used in later open water boundary computational experiments.

To test the use of a patched grid system on a closed rectangular basin with the depths given in figure 4, a force varying with space and time was imposed on the five-region closed basin of figure 5. The force converged to and remained zero after 40 Δt units of time. The exact nature of this force is not important to the experiment; it is only necessary to point out that it was not a function of depth and was concentrated near the shore midway between the upper and lower boundaries. The fluid of the basin oscillated freely until a total of 200 Δt time intervals elapsed. The total energy of the basin was monitored at each time step. Figure 6 illustrates the status of this energy consisting of a gradual rise with time (6 percent at the end of the experiment). Although the energy was not constant and changed during free oscillation of the rotating basin, the growth was not explosive.

Consider a small segment of a long coast struck by a severe storm, and focus attention on a small open section of the ocean traversed by the severe storm and containing the coastal segment as a closed boundary. If it is assumed that the sea level in this small section of the ocean, during the transient phase of the developing storm surge, changes predominantly as a local response to the force terms, then

the arbitrary positioning of open or closed boundaries on an extended area of the small ocean section should have little effect on the highly interesting, transient surge about the small coastal segment. This conclusion will be investigated in a later section by comparing results for a small coastal segment from calculations on a large closed basin with those on a smaller open basin.

6. COMPUTATIONS WITH THE WIND STRESS FUNCTIONS

If reasonable grid spacing is to be used in shallow water, it is hopeless to accommodate an entire ocean with today's computers even with the use of the patched grid system. Because the storm surge usually attains maximum values at the coastal region in the immediate vicinity of a storm's core slightly after storm passage, a small area of the ocean is presumed to be adequate for calculations of the transient surge on the coastal segment.

The five-region closed basin of figure 5 was used in an experiment using the wind stress functions of Appendix I (equation (18)). Although the closed basin is only a small fraction of the ocean and has three fictitious closed boundaries, the general features of the coastal storm surge midway between the upper and lower boundaries are sufficiently well portrayed during passage of a tropical storm. Comparisons were made between this master run and a separate identical run for a much smaller basin (broken line two-region sub-basin of fig. 5) with three open boundaries. The agreement of the two runs suggests that open boundary basins consisting only of the continental shelf extended along the shore may be sufficient for calculating the transient phase of the developing storm surge about a segment of the shore line.

One open boundary condition was zero height values on the open right boundary in deep water. Taking zero height values in deep water is a reasonable assumption borne out by theoretical and observational results which demonstrate that the storm surge from wind stress is inversely proportional to the depth (Defant [1]). This open right boundary condition is for the wind stress only and a separate condition is necessary when pressure is considered.

On the upper and lower open boundaries the depths run from the shallowest to the deepest water; consequently zero heights on these boundaries would not be applicable because of the shallow water near the shores. The field values in closed basins between the center of a storm and the upper and lower closed boundaries give considerable transport values from the left to right boundaries, and significant height values in shallow water which decrease to zero in deep water. It was decided from inspection of the transport field, and as a matter of convenience, to adopt on the upper and lower open boundaries the condition of vanishing normal derivative of transport, $\partial V/\partial y = 0$. This permits transport across the boundaries that is found empirically not to differ radically during the
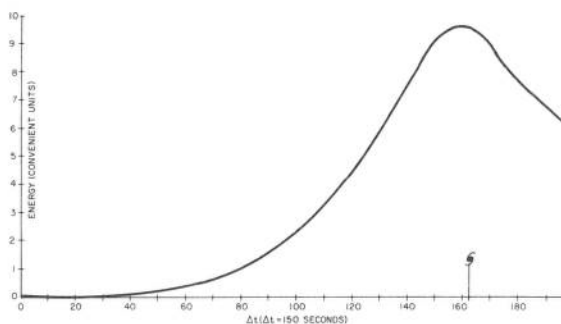

FIGURE 7.—Energy curve, in convenient units, with time for the closed five-region basin of figure 5 during action of the circular wind stress function. The storm crosses the coast at $162\Delta t$.

developing storm surge in sense and value from that of a much larger closed basin, providing these open boundaries are far removed from the storm center.

After calculating field values at all interior points, including the unsmoothed interior partition points, a sequence of calculations was made for the boundaries of the open basin as given in Appendix III.

The storm used in this experiment, relative to the closed basin of figure 5 was centered initially 202 mi. to the right of the left boundary and 132 mi. from the bottom boundary; its motion was to the left at 30 m.p.h. The constants for this storm (Appendix I) were $V_R = 100$ m.p.h., $R = 15$ mi., $k = 3 \times 10^{-6}$. The growth time for the storm was $40\Delta t$ ($\Delta t = 150$ sec.). The storm crossed the coast at $162\Delta t$. Ingress angle and storm motion effect were not considered in this first experiment.

Figure 7 gives the energy content with time for the above storm in the closed basin. Figure 8 gives contours of height for various times, comparing runs in the closed and open boundary basins. The displayed contours are restricted to the area of the open boundary basin of figure 5.

Figure 9 compares the height values at the coast itself for various times of these two runs. The curves are oriented so that the observer is facing seaward.

On the assumption that the open boundary basin containing a small shore segment can be used, providing the open boundaries are sufficiently far removed from the area of interest, further experiments were conducted to compare results for wind stress functions utilizing ingress angle and storm motion effects developed in Appendix I. The open boundary basin with two regions was extended in length from 136 to 200 mi.; its width remained 58 mi. The storm was centered initially 202 mi. from the left boundary and 88 mi. from the bottom open boundary. The storm constants remained the same and a constant ingress angle of 30° was chosen.

Three runs were performed on this open boundary basin for storms as follows: (1) circular winds only; (2) circular winds and ingress angle only; (3) circular winds, ingress angle, and storm motion effect. Figure 10 gives the height values for these three separate runs at various times on the coastal segment. The solid line is for run 3,
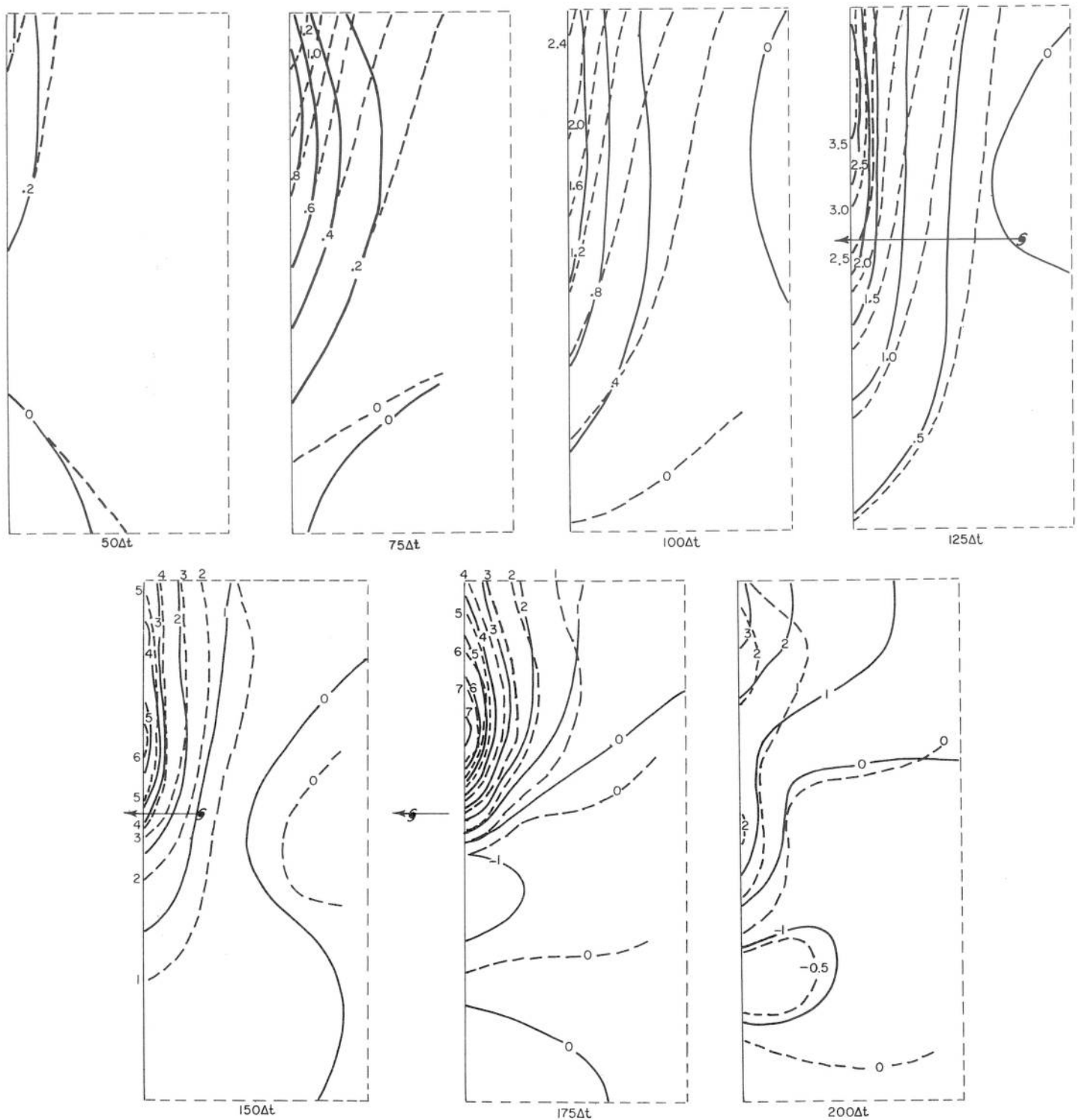
FIGURE 8.—Comparison of water height values in feet for various times with passage of a tropical storm in a closed and open boundary basin. The area of the display is the two-region sub-basin of figure 5. The solid contours are for the corresponding area of the five-region closed basin; the broken contours for the sub-basin. The force action is the wind stress function. The storm crosses the coast at $162\Delta t$. $\Delta t = 150$ sec.

the broken line is for run 2, and the dot-dashed line is for run 1. (Note that run 1 differs but slightly from the broken line run of figure 9 in spite of the coastal length differences in the two runs.) Of immediate significance

is the strong effect of the constant 30° ingress angle; the introduction of this angle gave more than a 60 percent rise of the maximum surge at the coast. The action of storm motion effect (stronger winds to the right relative
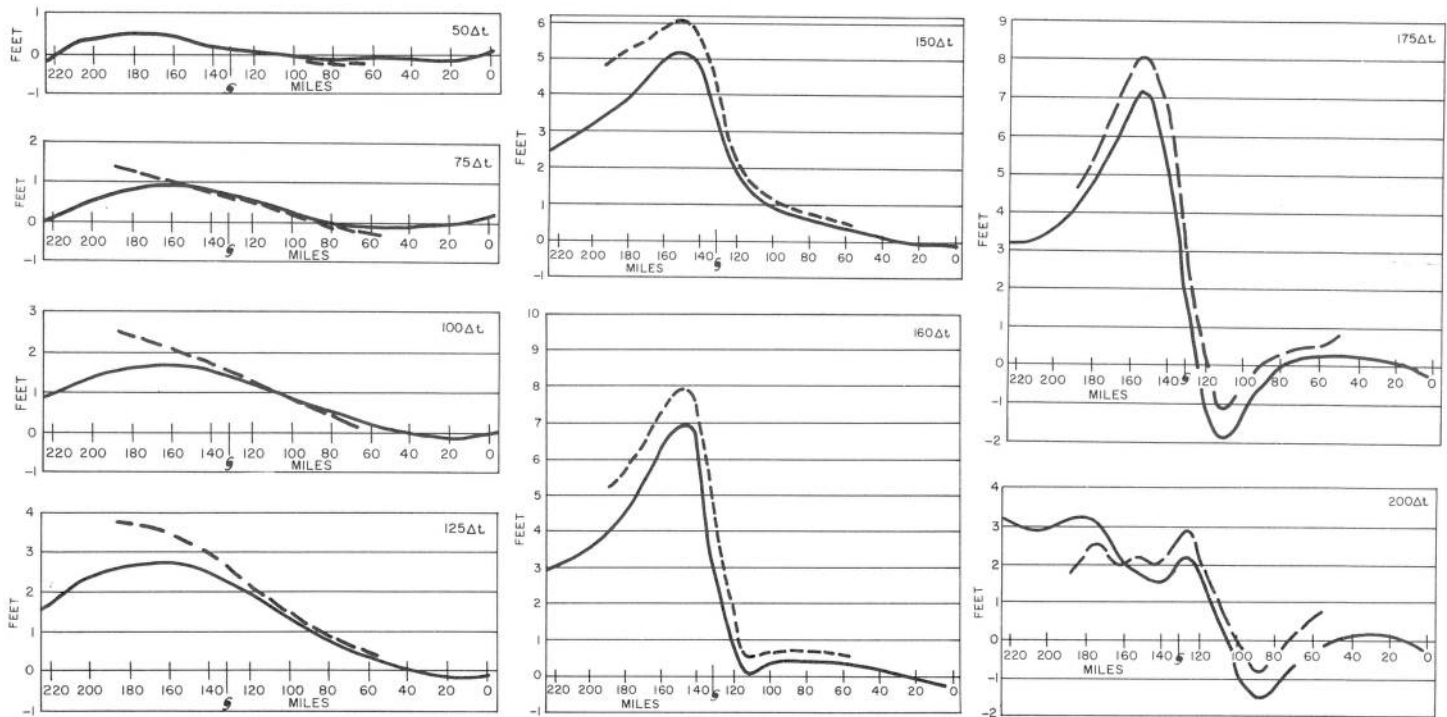
FIGURE 9.—Comparing water height values for various times along the coasts of the closed and open boundary basins of figure 5. The data were extracted from the calculations that produced figure 8. The observer is on land facing the sea. The storm strikes the coast 132 mi. from the bottom boundary of the closed basin. $\Delta t = 150$ sec.

to the storm's motion) while of significance is much smaller than that of the ingress angle; the maximum surge at the coast rose less than 7 percent between run 2 and run 3.

7. COMPUTATIONS WITH THE PRESSURE FORCE FUNCTION

In another set of calculations some aspects of the pressure force function (Appendix II) were investigated. The constants for the model storm generating the pressure force function were those of the previous section and a pressure difference $(p_\infty - p_0) = 45$ mb. between the center and a great distance was chosen. Figure 11 illustrates the static height of the basin's surface and the surface pressure of this storm with distance from the center.

Experience has shown that the pressure force function is more difficult to apply in numerical computations than the wind stress function when transport is used as a field value. It appears that the pressure force function, in a variable depth basin, has some troublesome properties that require modification of the numerical calculations presented thus far. When the pressure force function was applied to the five-region closed basin of figure 5, the results were hopelessly inadequate. Decreasing the regions, in order to form smaller mesh lengths in deep water, gave some improvement but the results were still inadequate. When the force function was smoothed in the calculations themselves, there was marked improvement. The numerical scheme for interior points of the momentum equations finally adopted was,

$$U_{i,j}^{m+1} = U_{i,j}^{m-1} - gD_{i,j}\frac{\Delta t}{4\Delta s}\begin{vmatrix} -1 & 0 & 1 \\ -2 & 0 & 2 \\ -1 & 0 & 1 \end{vmatrix} h_{i,j}^m$$

$$+ \frac{\Delta t}{8}\begin{vmatrix} 1 & 2 & 1 \\ 2 & 4 & 2 \\ 1 & 2 & 1 \end{vmatrix} (fV_{i,j}^m + {}^{(x)}\tau_{i,j}^m) \quad (13)$$

where ${}^{(x)}\tau$ is now the pressure force function. A similar scheme holds for the V transport.

Even though the use of (13) was an improvement over (4), it was found that the five-region closed basin gave unfavorable results. This means that the pressure force function, in a variable depth basin, is less forgiving than the wind stress in numerical computation when transport terms are used. Limitations of the program allowed a master run for a one-region closed basin (fig. 12) with grid spacings of 5 mi. and a Δt of 30 sec. The storm was initially positioned 200 mi. from the left boundary and 130 mi. from the bottom closed boundary. The depths were those of figure 4. For this run, the force function was smoothed only at interior points and not at boundary points. The contours of field values were generally smooth and continuous except at the end of the run when the patterns started to show signs of fragmentation.

Figure 13 illustrates the energy of the closed basin with time. Notice that kinetic energy is small compared to potential energy until the storm's center invades the shallow continental shelf. Not until the storm passes the coast does kinetic surpass potential energy. This suggests that the core of the storm when in deep water and distant
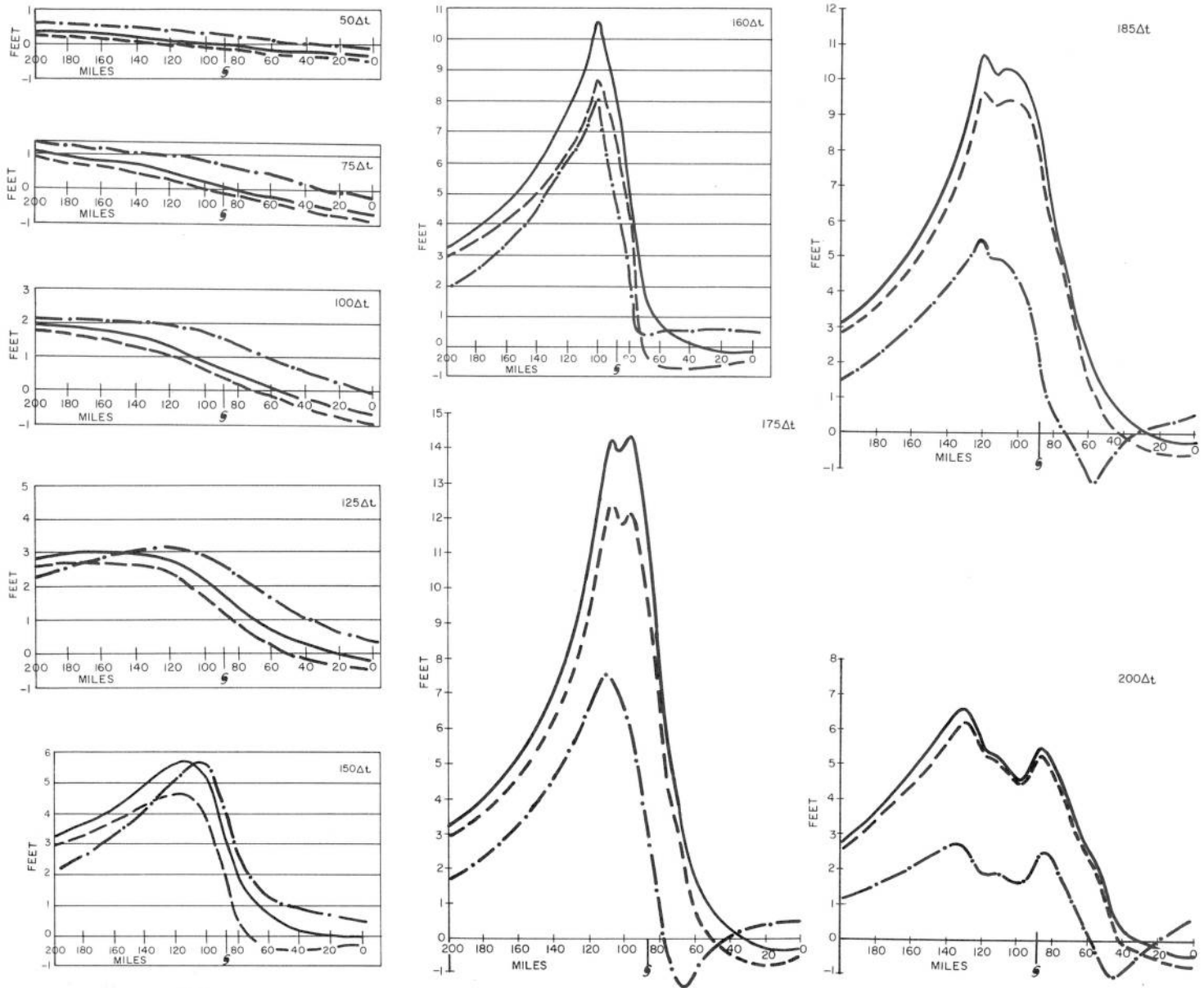
FIGURE 10.—Comparison of height values for various times along the coast of an open boundary basin acted on by the wind stress function for three runs: 1. Circular winds only (dot-dashed line).   2. Circular winds and an ingress angle of 30° (dashed line).   3. Circular winds, an ingress angle of 30°, and storm motion effects (solid line).   The observer is on land facing the sea.   The storm crosses the coast 88 mi. from the bottom boundary.   The dot-dashed curves are similar to the open boundary curves of figure 9 except for coastal length differences. $\Delta t = 150$ sec.

from the coast merely elevates the surface hydrostatically, whereas when it is moving across the sloping depth, reflection of the elevated mound of water becomes possible.

The solid contours of figure 12 denote the water elevation for this run at time 250 Δt.   About the center of the storm, the elevation agrees almost exactly with that of the static height (fig. 11) but begins to diverge and even have slight negative elevation at distances from the storm center.   This is to be expected in order to conserve mass continuity in the closed basin.

The solid line of figure 14 depicts the water elevation with time at the coastal point crossed by the storm's
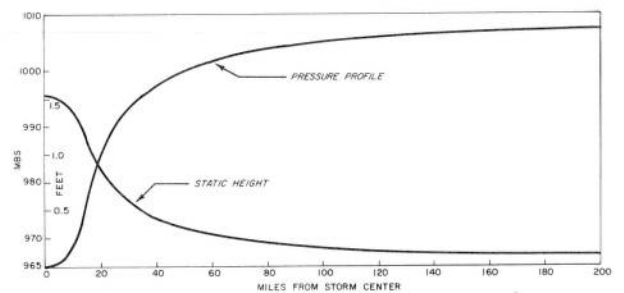
FIGURE 11.—The surface pressure (mb.) and static height (ft.) with distance from the storm's center.   This model storm was used for calculating the pressure force function.
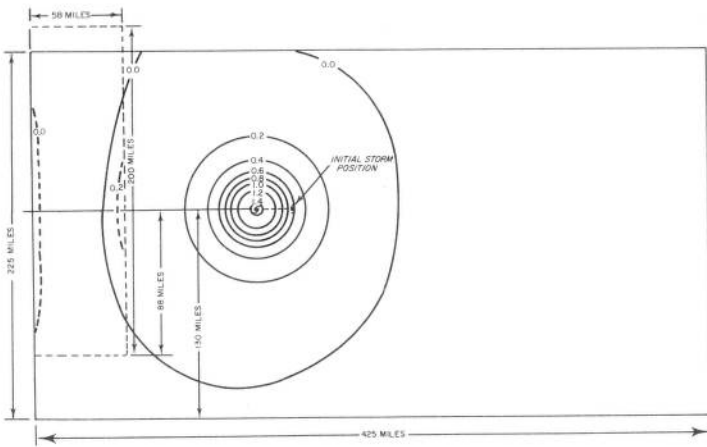
FIGURE 12.—Comparison of height values in feet in a one-region closed basin and a two-region open basin when the pressure force function only is active. The broken line area is the open basin placed in position relative to the closed basin. Different time intervals were used in the basins. Time is $250\Delta t$ ($\Delta t=30$ sec.) for the closed basin, $50\Delta t$ ($\Delta t=150$ sec.) for the open basin.
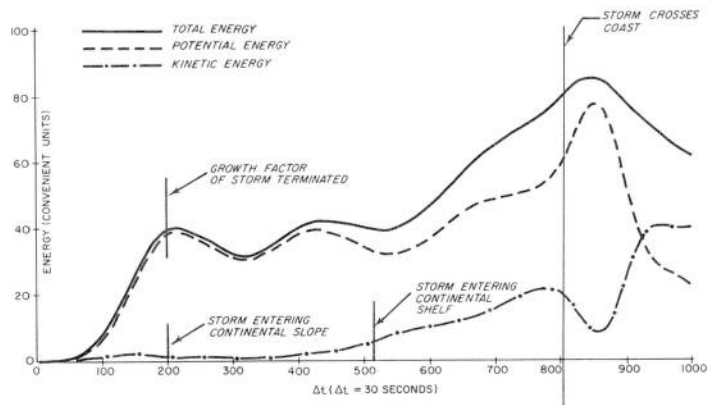

FIGURE 13.—Energy, in convenient units, with time for a one-region closed basin with passage of the pressure force function. The storm strikes the coast at $805\Delta t$ ($\Delta t=30$ sec.).

center. Little of consequence occurs at this point (and the entire coast) until the storm is near the coast. The maximum elevation is three times the static height. This implies that a simple proportional static height correction to the dynamic wind stress height may not be sufficient to describe the storm surge and that the dynamics of the pressure force function are significant in coastal regions (Robinson [8]).

To see how the pressure force function acts in an open boundary basin, the two-region sub-basin, with $\Delta s=2$ mi., of the previous section (or fig. 12) was chosen. The time increment Δt was 150 sec. compared to 30 sec. for the larger grid spaced one-region closed basin. The top and bottom open boundary condition of the wind stress function was used, $\partial V/\partial y=0$. A static height boundary condition was applied to the right boundary in deep water. This condition was chosen from results of the previous run in the much larger closed basin. The growth factor of the
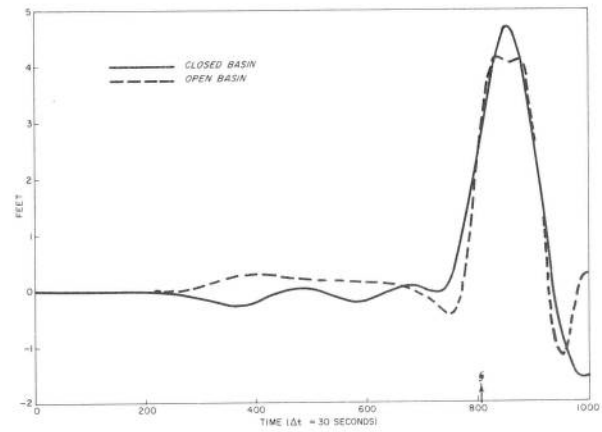

FIGURE 14.—Comparison of height values with time at the point of the shore crossed by the storm.

storm was applied to the pressure force function and to the static height value on the boundary. Transport on the right boundary was determined as in Appendix III, by the numerical form,

$$U_{I,j}^{m+1}=U_{I,j}^{m-1}+\frac{g\Delta t}{\Delta s}[4D_{I-1,j}(h_{I-1,j}^m-h_{I,j}^m)-D_{I-2,j}$$

$$(h_{I-2,j}^m-h_{I,j}^m)]+2\Delta t f\tilde{V}_{I,j}^m+\frac{\Delta t}{8}\begin{vmatrix}1 & 2 & 1\\2 & 4 & 2\\1 & 2 & 1\end{vmatrix}^{(x)}\tau_{I,j}^m \quad (14)$$

The pressure force function for this boundary was smoothed in the numerical calculations except for the corner points. This was possible since the pressure force was analytically described and could be determined at points beyond the right boundary. The force function was not smoothed on the other three boundaries.

On the partition line, the five-point smoothing forms of (10)–(11) were applied to smooth the force in the calculations.

Figure 15 compares the height values in the open and closed basins of figure 12. Contours are described for the area of the open basin. The times are in units of $\Delta t=150$ sec. Comparison of these two runs at the coastal point crossed by the storm's center is given in figure 14. The small difference of the two runs prior to the storm's arrival is attributed to the open right boundary condition which overemphasized the height values in the early stages. The double maximum of the open boundary run did not appear in a separate run for a one-region open boundary basin ($\Delta s=4$ mi.); this suggests that the reflecting mound of water may be a complex feature requiring smaller grid intervals for fuller interpretation.

Since the pressure force function is smoothed in the calculations, it was decided to test some runs with smoothed wind stresses. There were only slight differences in the storm surge for the basins and grid sizes used in this study for smoothed and unsmoothed wind stress functions.
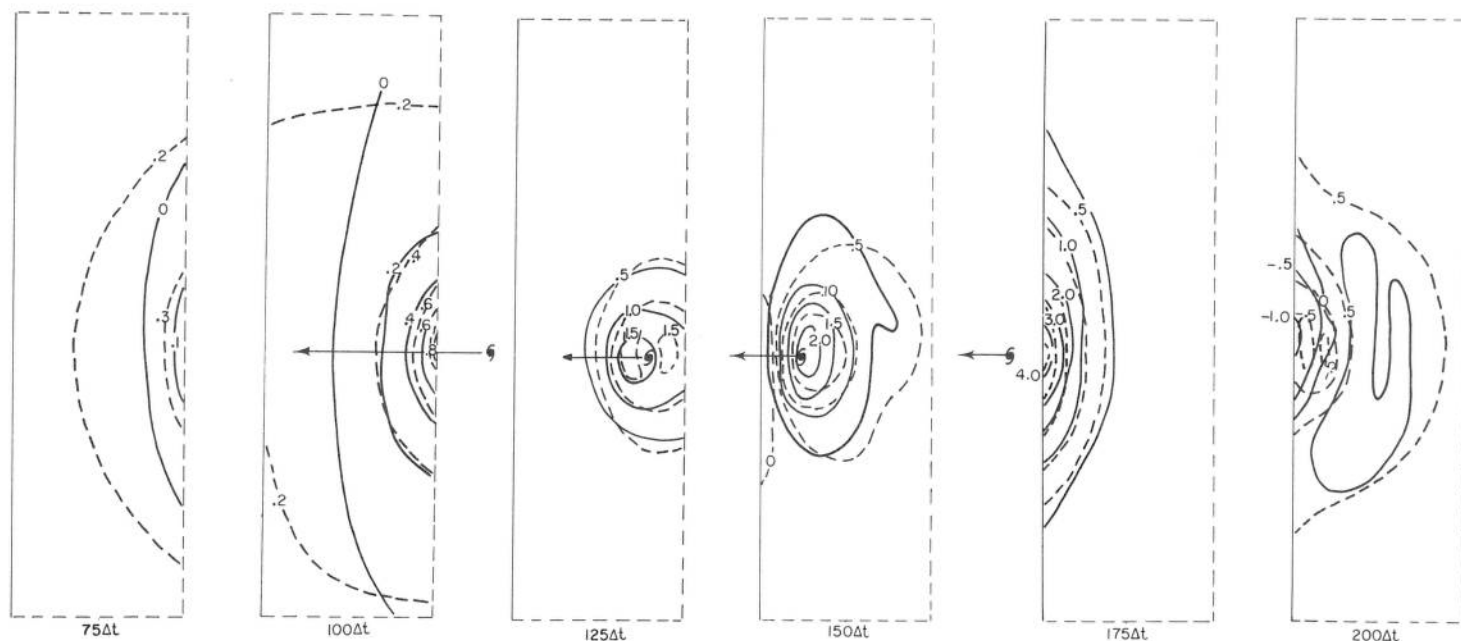
FIGURE 15.—Comparisons of height values (in ft.) with time for passage of the pressure force function in the basins of figure 12. The area displayed is the open basin of figure 12. The solid contours are for the closed basin, the broken contours for the open basin. $\triangle t = 150$ sec.

8. SUMMARY AND CONCLUSIONS

The forcing functions of a tropical storm are predominant in controlling storm surges at a coastal region, whereas initial values are of such minor importance that the sea can be considered initially quiescent. The important storm parameters responsible for generating storm surges are insufficiently described by present meteorological data. In order to gather insight into the prediction problem, idealized storms that incorporate recognized storm parameters have been analytically described.

It is convenient to describe the storm from considerations presumed to hold at and near its center where the wind and pressure gradient are greatest, and to ignore other effects. The resulting discrepancy at large distances from the storm's center, where the wind and pressure gradients are small, affects the maximum coastal surge only in a minor sense.

In nature, the storm generally is positioned initially at great distances from shore and reaches maturity after several days have elapsed; in this study the storm was initially placed relatively close to shore and reached maturity quickly. This choice is justified when it is realized that the sea's surface does not elevate dramatically until the mature storm approaches the coast. Test runs with the same storm placed initially between 150 and 250 mi. from the coast, with all other factors remaining the same, resulted in very little differences of the maximum coastal sea elevations among the runs.

The wind stress is applied only at the surface and is independent of the basin's depth. The resulting water elevation from the wind stress is much larger in shallow than in deep water. The elevations are asymmetric about the storm's center; higher seas occur to the right of the storm's path (observer facing land). The maximum sea elevation at the coast occurs not at the time of storm passage, but slightly after the storm strikes the coast.

The circular wind stress in elementary form was modified with a constant ingress angle throughout thereby curving the tangential wind toward the storm's center, and also by a variable correction to the wind vector depending on the storm's motion. The ingress angle was highly significant for the storm studied. A more elaborate technique that describes a variable ingress angle in the storm may give further insight to storm surge generation. The effect from storm motion, while of academic interest, was much smaller in scope than that from the ingress angle.

The pressure gradient acts radially to the storm's center; the vertically integrated form of this force, the pressure force function, is a function of depth. The elevation of water by this force function is mostly static in deep water and forms a raised mound of water immediately under and following the core of the storm until reflected by the coast. The mound of water is almost symmetric about the storm with very little displacement of maximum height values to the right of the storm's path. The reflection of the water mound at the coast gave a maximum sea elevation three times that of the static height for the storm studied and occurred slightly after the storm struck the coast.

If computer memory space and computation time are serious factors to be considered, then regions of differing grid sizes in a basin may be used for the transient phase of the generating storm surge. For the model basin of this study, initial values play a minor role, the dynamic surge is small throughout except at the shallow shore restricted to the storm's core or central area regardless of the storm's size and strength, and the shallow shore water does not begin surging alarmingly until the approach of the storm's core. Consequently, sub-basins with open boundary conditions were used to calculate the sea's response at a coastal strip crossed by the storm.

In deep water, elevation of the water surface occurs mainly from the pressure force function in the static sense; hence it was natural to assume static heights as a boundary condition in deep water.

Vanishing normal derivative of transport was used as a condition on the other open boundaries with the proviso that the boundaries remain distant from the core of the storm. This open boundary condition permits a closed system of numerical forms to operate on a sub-basin of the ocean basin. The condition, while untrue in a strict physical sense, was formulated in regions of little dynamic storm surge activity.

A storm will cross at least one open boundary of a small sub-basin. It is desirable to position the sub-basin in such a manner that the storm crosses an open boundary in deep water so that static height conditions can be applied thereon. The remaining open boundaries can then be placed at distances from the storm's path.

The storm in this report crossed the coast at normal incidence, but it is a simple matter to consider angular crossings of the coast. Should the angle of crossing be too large or should the storm follow a parallel path to the coast thereby preventing a deep water boundary crossing, then a modification of the numerical scheme may be required. One could begin in this case by initially positioning and orienting the sub-basin in that part of the ocean where the storm would pass a deep water open boundary prior to the storm's recurvature. The basin could then leap-frog along the coast as the storm moves. Prior to each jump or leap-frog, historical field values for selected interior points of the upper basin would be retained after each time step. As the sub-basin jumps to a new position, and the calculations begin anew, the historical field values of the selected points are then values supplied to the lower boundary of the newly positioned basin. With the sub-basin following the storm in this manner, the entire coastal region affected by the storm can be described. The study of coastal storm surges for differing storm motions, sizes, and strengths is deferred to the future.

In this study, no attempt was made to predict quantitative height values for operational use, nor to compare them with observed values, since bottom stress, curvilinear boundaries, and nonlinear effects in shallow water were not considered. The contents are only exploratory in order to gain insight. Restriction to a qualitative appraisal of coastal storm surges with the aid of idealized storms and basins is a reasonable procedure at present.

APPENDIX I—WIND STRESS FUNCTION

It is desirable to formulate wind stresses that act on a sea surface in analytical form which approximates the passage of a tropical storm. Consider a circular storm, symmetric in wind speed about its center, with maximum winds V_R at distance R from its center. Let it be assumed that the wind speed V at a distance r from the center is

$$V = V_R \left(\frac{r}{R}\right)^{3/2}, \qquad 0 \leq r \leq R \qquad (15)$$

$$V = V_R \left(\frac{R}{r}\right)^{1/2}, \qquad r \geq R \qquad (16)$$

Figure 16 is a comparison of the above wind speeds with those of the August 1949 storm as described in [9].

The computation of surface stress from wind data is a controversial subject. In this study it is assumed that the quadratic stress law holds for the sea surface as a result of the action of the wind $\mathbf{V}$ so that,

$$\tau = k|\mathbf{V}|\mathbf{V}; \; k = \frac{K\rho_a}{\rho} \qquad (17)$$

where K is a stress constant, ρ_a and ρ are air and water density.

In a hurricane, the wind in general is directed across the isobars into the interior of the storm. This ingress angle varies in space and time. Since interesting features are sought, the ingress angle ϕ in this paper will be assumed constant throughout the storm for initial purposes of convenience. In figure 17 where ϕ is the ingress angle, θ the polar angle, the components of surface stress are,

$$^{(x)}\tau = -kV^2 \sin(\theta + \phi); \; ^{(y)}\tau = kV^2 \cos(\theta + \phi) \qquad (18)$$

After substitution of (15) and (16) into (17) the components become

$$^{(x)}\tau = kV_R^2 \frac{r^2}{R^3} A; \; ^{(y)}\tau = kV_R^2 \frac{r^2}{R^3} B, \qquad 0 \leq r \leq R \qquad (19)$$

$$^{(x)}\tau = kV_R^2 \frac{R}{r^2} A; \; ^{(y)}\tau = kV_R^2 \frac{R}{r^2} B, \qquad r \geq R \qquad (20)$$

where, $A = -y \cos\phi - x \sin\phi$; $B = x \cos\phi - y \sin\phi$.

In a hurricane, the winds are not necessarily of constant speed on equal radii from the center of the storm. On the contrary, higher speeds in general favor the right side of the storm relative to its direction of motion. In this discussion, the naive view is taken that the motion of the storm affects the surface wind as a function of position with respect to the storm center. An additional wind velocity $\mathbf{V}_{SM}$ is thus added to the circular wind velocity.
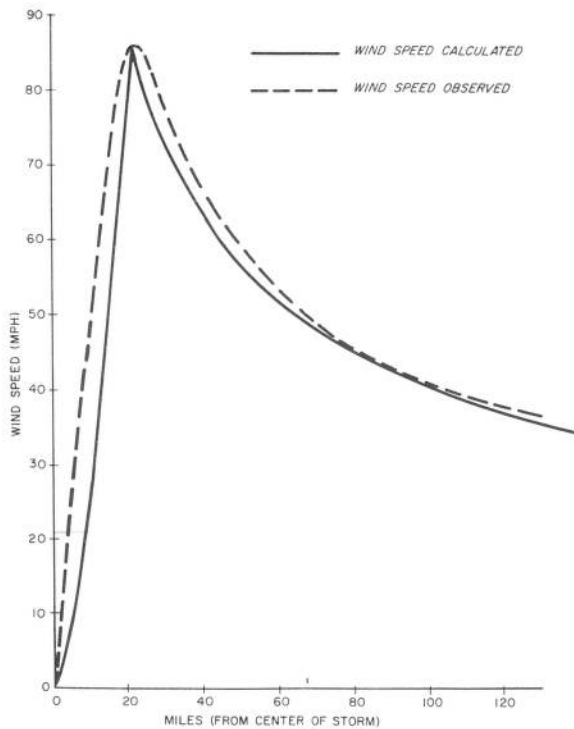
FIGURE 16.—Comparison of calculated vs. observed wind speeds with distance from a storm's center. The observed values were obtained from the August 1949 storm [9].

Consider figure 17c, where $\mathbf{U}_S$ is the velocity of the storm center with components U_S and V_S. The additional wind velocity $\mathbf{V}_{SM}$ is taken as,

$$\mathbf{V}_{SM}=\frac{r}{R+r}\,[U_s\mathbf{i}+V_s\mathbf{j}], \qquad 0\leq r\leq R;$$

$$\mathbf{V}_{SM}=\frac{R}{R+r}\,[U_s\mathbf{i}+V_s\mathbf{j}], \qquad r\geq R \qquad (21)$$

where, $\mathbf{i}$, $\mathbf{j}$ are unit vectors on the coordinate axis. The surface wind is now defined as,
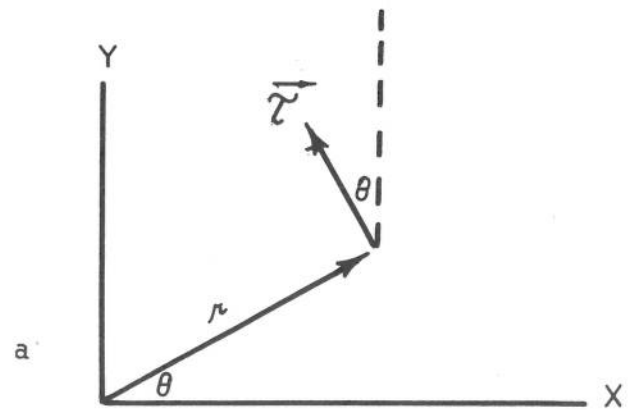
$$\mathbf{V}^*=\mathbf{V}+\mathbf{V}_{SM} \qquad (22)$$

The surface stress conforming to (17) now has the adjusted wind velocity $\mathbf{V}^*$, or,

$$\boldsymbol{\tau}=k|\mathbf{V}^*|\mathbf{V}^*=k|\mathbf{V}+\mathbf{V}_{SM}|(\mathbf{V}+\mathbf{V}_{SM}) \qquad (23)$$
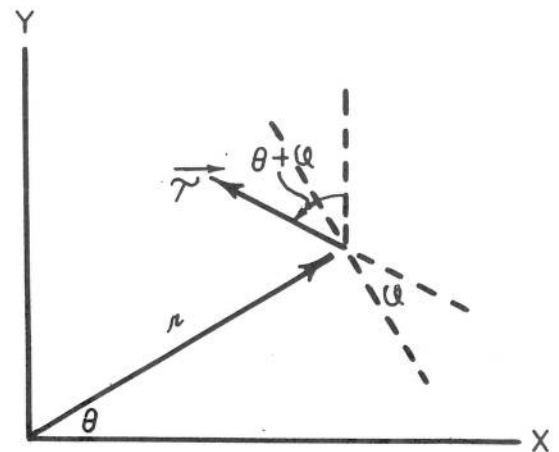
Consider the wind velocity corrected for ingress angle ϕ; then in vector components,

$$\left.\begin{aligned}\mathbf{V}&=V_R\left(\frac{r}{R}\right)^{3/2}\frac{1}{r}\,[A\mathbf{i}+B\mathbf{j}]; & 0\leq r\leq R\\[2mm]\mathbf{V}&=V_R\left(\frac{R}{r}\right)^{1/2}\frac{1}{r}\,[A\mathbf{i}+B\mathbf{j}]; & r\geq R\end{aligned}\right\} \quad (24)$$
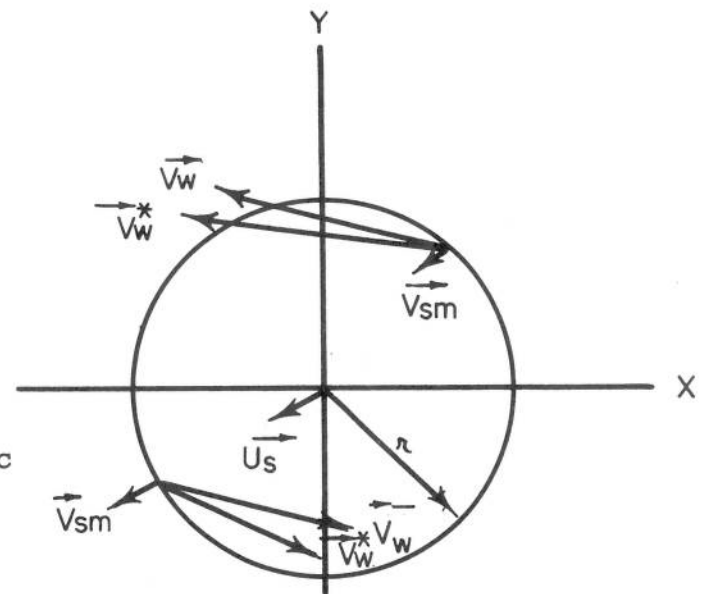
Substituting (21) and (24) into (23) gives the vector form of wind stress that considers ingress angle and storm

FIGURE 17.—(a) The wind stress direction for a circular force function. (b) The wind stress direction for a circular force function with ingress angle ϕ. (c) The vector addition of the storm motion effect vector $\mathbf{V}_{SM}$ to the wind vector $\mathbf{V}$.

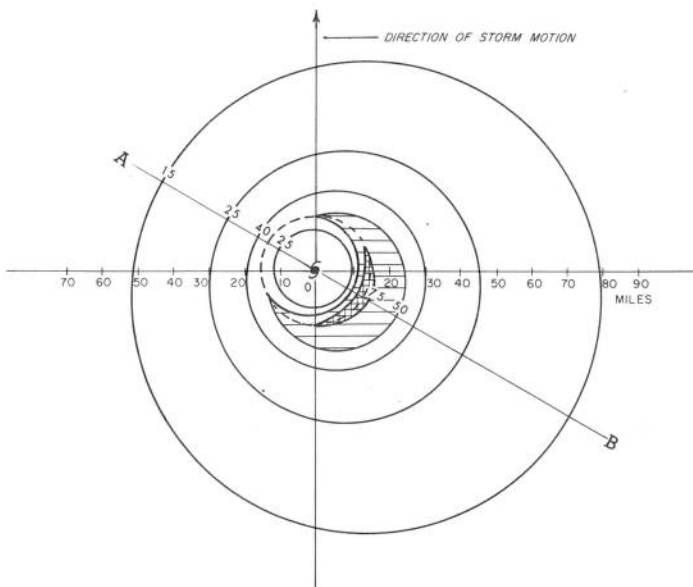FIGURE 18.—The magnitude, in convenient units, of the wind stress function about a storm considering the effects of ingress angle 30°, and storm motion 30 m.p.h. The line AB is oriented 30° clockwise from the abscissa; it passes through the center of the storm and the maximum wind stress. The broken circle is the radius (15 mi.) of the maximum wind.

motion effect. Figure 18 illustrates the magnitude of wind stress contours in convenient units for a storm with the constants, $V_R=100$ m.p.h., $R=15$ mi., $V_{SM}=30$ m.p.h., $\phi=30°$. Equation (23), although formidable in appearance, increases the computation time of the total program very little compared to the computation time using simple circular winds.

The forcing function (stress in this case), initially quiescent, is allowed to grow with time by multiplication with the following function of time,

$$F(t)=0, \qquad t\leq 0$$

$$F(t)=\tfrac{1}{2}(1-\cos(\pi t/T)), \qquad 0\leq t\leq T$$

$$F(t)=1, \qquad t\geq T$$

where T is the growth time.

APPENDIX II—THE PRESSURE FORCE FUNCTION

Consider a circular storm, symmetric in wind speed about the center, with maximum winds V_R at distance R from the center. The pressures p_0 at the center and p_∞ at great distance from the center are assumed known. Let it be further assumed that cyclostrophic wind reigns in that part of the storm of greater interest in storm surges when friction is absent. Then,

$$\frac{1}{\rho_a}\frac{\partial p}{\partial r}=\frac{V_c^2}{r} \qquad (25)$$

where V_c is the cyclostrophic wind, r the distance from

the storm center, and ρ_a the air density (1.173×10^{-3} gm. /cm.³). Unfortunately, the cyclostrophic wind differs substantially from the surface or near surface wind, in large measure because of friction. It will be assumed that the surface or near surface wind V is proportional to the cyclostrophic wind.

Then,

$$V=\gamma V_c \qquad (26)$$

where γ is to be determined.

Replacing V_c in (25) by (26) is a convenience to eliminate the necessity of formulating surface friction terms. Inserting the surface wind (Appendix I) into (25) gives,

$$\frac{\partial p}{\partial r}=\rho_a\left(\frac{V_R}{\gamma}\right)^2\frac{r^2}{R^3}, \qquad 0\leq r\leq R \qquad (27)$$

$$\frac{\partial p}{\partial r}=\rho_a\left(\frac{V_R}{\gamma}\right)^2\frac{R}{r^2}, \qquad r\geq R \qquad (28)$$

Integrating the above gives

$$p=\frac{\rho_a}{3}\left(\frac{V_R}{\gamma}\right)^2\left(\frac{r}{R}\right)^3+p_0, \qquad 0\leq r\leq R \qquad (29)$$

$$p=-\rho_a\left(\frac{V_R}{\gamma}\right)^2\frac{R}{r}+p_\infty, \qquad r\geq R \qquad (30)$$

Eliminating p and setting $r=R$,

$$p_\infty-p_0=\frac{4}{3}\rho_a\left(\frac{V_R}{\gamma}\right) \qquad (31)$$

Note that by this formulation, one fourth of the storm's pressure difference [1] $(p_\infty-p_0)$ occurs between the storm center and the radius of maximum winds. Equation (31) permits a determination of γ at $r=R$ to be,

$$\gamma=2V_R\sqrt{\rho_a/3(p_\infty-p_0)} \qquad (32)$$

The coefficient γ is taken as constant throughout the storm in this study. This method of determining γ is a convenience to allow the use of a simple expression which portrays the major features of the storm's pressure gradient. In no way is it suggested that this is an adequate formulation of the surface friction (Myers [6]).

Figure 19 gives sea level pressure values extracted from [9] observed and computed from the standard pressure formula $(p-p_0)/(p_\infty-p_0)\equiv \exp(-R/r)$ compared to that obtained from (29) and (30). Except to say that (29) and (30) are more tractable for machine computations, no inference is drawn that they are in any way superior to the standard pressure formula. The values used in the computations are $(p_\infty-p_0)=60$ mb., $V_R=86$ m.p.h., and $R=22$ mi.

---

[1] It is possible to arrive at a greater ratio by a minor reformulation of the wind equation. For a linear wind increase with distance from the storm center to the radius of maximum wind, (31) becomes $(p_\infty-p_0=\tfrac{3}{2}\rho_a(V_R/\gamma)^2$; here the difference is now ½.
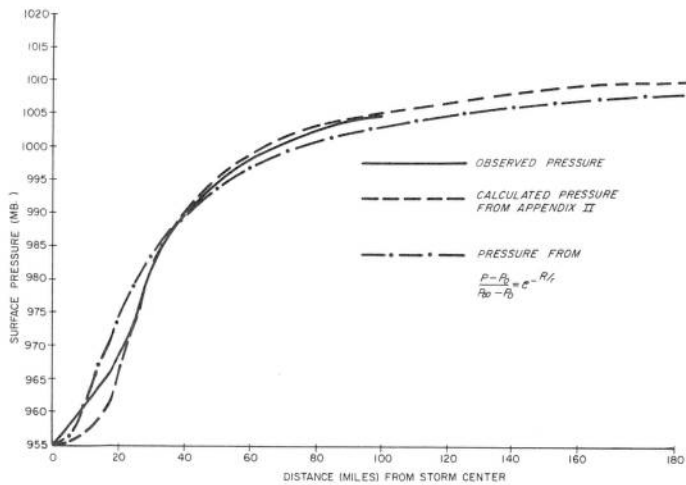
FIGURE 19.—Comparison of calculated vs. observed surface pressure with distance from the storm's center.

The pressure force function τ_p in linear form from [3] is

$$\tau_p = -\frac{D(x,y)}{\rho}\,\nabla p \qquad (33)$$

In component form, through (27) and (28), this becomes,

$$^{(x)}\tau_p = -\frac{\rho_a}{\rho}\frac{D}{R^3}\left(\frac{V_R}{\gamma}\right)^2 rx;\quad ^{(y)}\tau_p = -\frac{\rho_a}{\rho}\frac{D}{R^3}\left(\frac{V_R}{\gamma}\right)^2 ry$$

$$0 \le r \le R$$

$$^{(x)}\tau_p = -\frac{\rho_a}{\rho} DR\left(\frac{V_R}{\gamma}\right)^2 \frac{x}{r^3};\quad ^{(y)}\tau_p = -\frac{\rho_a}{\rho} DR\left(\frac{V_R}{\gamma}\right)^2 \frac{y}{r^3},$$

$$r \ge R \qquad (34)$$

These are the pressure force functions. No attempt is made to modify these equations for ingress angle or storm motion effects since experience shows that the pressure force function contributes much less to the storm surge in shallow water than the surface wind stress and that the pressure gradient is predominantly displayed by the circular wind assumption.

It is interesting to compare the pressure force function and wind stress for magnitude. For circular winds, the maximum wind stress occurs at $r=R$. The ratio of pressure force function to wind stress (Appendix I) at $r=R$ is,

$$\frac{|\tau_p|}{|\tau|_{r=R}} = \frac{\rho_a D}{\gamma^2 k R}, \qquad r=R \qquad (35)$$

For the August 1949 storm, depths of 15 and 10,000 ft. give ratios of 0.13 and 87.5 respectively. This shows that the wind stress has greater magnitude in shallow water while the pressure force function has greater magnitude in deep water.

APPENDIX III—SEQUENTIAL CALCULATIONS OF THE BOUNDARY POINTS

To calculate the field values on the boundary points, the following sequence was followed in the computations:

1. The transport V on the left closed boundary, excluding corners, using the central difference form. Since U is zero on this boundary, the Coriolis cross term is omitted.

2. The transport V on the right open boundary, excluding corners, using the central difference form. The Coriolis cross term[2] is retained since transport U does occur on the open boundary.

3. The transport U on the upper and lower open boundaries, excluding corners, using the central difference form. The Coriolis cross term[2] is retained.

4. The transport U on the open right boundary, including the two corner points, by the following numerical form that uses interior points,

$$U^m_{I,j} = U^{m-1}_{I,j} + g\frac{\Delta t}{\Delta s}\left(4D_{I-1,j}h^m_{I-1,j} - D_{I-2,j}h^m_{I-2,j}\right)$$
$$+ 2\Delta t\left(fV^m_{I,j} + {}^{(x)}\tau^m_{I,j}\right) \quad (36)[3]$$

where I is the abscissa of the right boundary, and $\tilde{V}$ is the result of a three-point smoothing. (See footnote 2.) Conceptually, one could use a central difference form, or a modified form here by assuming zero h not only for the boundary points but also for points beyond the boundary. Results indicate that for the wind stress function (36) is preferable.

5. The transport V on the upper and lower boundaries, including corners, from the boundary conditions, $\partial V/\partial y=0$, using interior points as follows,

$$V^m_{i,0} = (4V^m_{i,1} - V^m_{i,2})/3;\quad V^m_{i,J} = (4V^m_{i,J-1} - V^m_{i,J-2})/3 \quad (37)$$

where J is the ordinate of the upper boundary. The V transport on a partition line boundary point is calculated *after* the interior partition points have been smoothed. The interior partition points are smoothed *after* the boundary points, excluding the boundary partition point, are calculated.

6. The height value h on the upper and lower bounda-

---

[2] In this study, the Coriolis cross terms on open boundary points (excluding corners) are smoothed in the calculations by the three-point form,

$$\tilde{V}^m_{i,j} = \frac{1}{4}\begin{vmatrix}1\\2\\1\end{vmatrix} V^m_{i,j}$$

[3] (36) is arrived at by forming

$$D\frac{\partial h}{\partial x} = \frac{\partial}{\partial x}(Dh) - h\frac{\partial D}{\partial x}$$

in the equations of motion and using the finite difference form,

$$\frac{d(\ )}{dx} = \frac{1}{2\Delta s}[3(\ )_I - 4(\ )_{I-1} + (\ )_{I-2}].$$

ries, excluding corners, using the central difference form on the continuity equation, $\partial h/\partial t = -\partial u/\partial x$.

7. The h value on the left boundary, including corners, by means of equation (7) of the study.

REFERENCES

1. A. Defant, *Physical Oceanography*, vol. II, Pergamon Press, New York, 1961, 598 pp. (pp. 235–237).
2. W. Hansen, "Theorie zur Errechnung des Wasserstandes und der Strömungen in Randmeeren nebst Anwendungen," *Tellus*, vol. 8, No. 3, Aug. 1956, pp. 287–800.
3. D. L. Harris and C. Jelesnianski, "Some Problems Involved in the Numerical Solutions of Tidal Hydraulics Equations," *Monthly Weather Review*, vol. 92, No. 9, Sept. 1964, pp. 409–422.
4. M. Miyazaki, T. Ueno, and S. Unoki, "Theoretical Investigations of Typhoon Storm Surges Along the Japanese Coast," *Oceanographic Magazine*, vol. 13, No. 1, Nov. 1961, pp. 51–75, and No. 2, Mar. 1962, pp. 103–107.
5. M. Miyazaki, "A Numerical Computation of the Storm Surge of Hurricane Carla 1961 in the Gulf of Mexico," *Technical Report* No. 10, to U.S. Weather Bureau, Dept. of Geophysical Science, University of Chicago, 1963.
6. V. Myers and W. Malkin, "Some Properties of Hurricane Wind Fields as Deduced from Trajectories," *National Hurricane Research Project Report* No. 49, U.S. Weather Bureau, 1961, 45 pp.
7. G. Platzman, "The Prediction of Surges in the Southern Basin of Lake Michigan—Part I. The Dynamical Basis for Prediction," *Monthly Weather Review*, vol. 93, No. 5, May 1965, pp. 275–281.
8. A. Robinson, "Continental Shelf Waves and the Response of Sea Level to Weather Systems," *Journal of Geophysical Research*, vol. 69, No. 2, Jan. 15, 1964, pp. 367–368.
9. R. Schloemer, "Analysis and Synthesis of Hurricane Wind Patterns over Lake Okeechobee, Florida," *Hydrometeorological Report* No. 31, U.S. Weather Bureau, 1954, 49 pp.
10. F. Shuman, "Numerical Methods in Weather Prediction: II. Smoothing and Filtering," *Monthly Weather Review*, vol. 85, No. 11, Nov. 1956, pp. 357–361.